

# Effect of Current Density on the Properties of Ni–CeO<sub>2</sub> Composite Coatings prepared using Magnetic Field-Assisted Jet Electrodeposition

*Ren An-hua<sup>1</sup>, Fu Xiu-qing<sup>1,2,\*</sup>, Chen Xin-xin<sup>1</sup>, Lin Jin-ran<sup>1</sup>, and Cao Hong-bing<sup>1</sup>*

<sup>1</sup> College of Engineering, Nanjing Agricultural University, Nanjing 210031, P. R. China;

<sup>2</sup> Key laboratory of Intelligence Agricultural Equipment of Jiangsu Province, Nanjing 210031, P. R. China;

\*E-mail: [fuxiuqing@njau.edu.cn](mailto:fuxiuqing@njau.edu.cn)

*Received:* 1 August 2020 / *Accepted:* 29 August 2020 / *Published:* 30 April 2021

---

Ni–CeO<sub>2</sub> composite coatings with excellent performance were prepared using jet electrodeposition while reducing the adverse effects of surface defects in the coating due to the agglomeration of nano-CeO<sub>2</sub> particles. In the jet electrodeposition process, a vertical magnetic field was introduced to prepare Ni–CeO<sub>2</sub> composite coatings at different current densities. With the help of scanning electron microscopy, energy dispersive spectroscopy, and microhardness measuring instrument, the surface morphology, structure, and composition of the coatings were studied, respectively. Further tests were conducted on the friction, wear, and corrosion resistances of the coatings to explore the effect of current density on the comprehensive performance of the composite coatings prepared under a vertical magnetic field. The results showed that under the action of the magnetohydrodynamic effect produced by the magnetic field, the particles in the composite coatings are arranged regularly, and with the increase in the current density, the microhardness, wear resistance, and corrosion resistance first increased and then decreased. The composite coating prepared under a processing current density of 20 A/dm<sup>2</sup> exhibited a good surface density and flatness, with the microhardness value reaching a maximum of 665.78 HV<sub>0.1</sub>. Moreover, it exhibited the best wear and corrosion resistances.

---

**Keywords:** Magnetic field; Current density; Ni–CeO<sub>2</sub> composite coating; Wear resistance; Corrosion resistance

## 1. INTRODUCTION

A metal matrix composite (MMC), which is a composite material with an excellent performance, is prepared by adding different reinforcing phases [1, 2]. In recent years, it has been widely used in aerospace, automotive, electronics, and military fields. Among MMCs, nickel-based alloys have been

used in industrial production owing to their excellent performance and low price. Nanomaterials have better properties than micromaterials, including in terms of the hardness, stiffness, and optical, electrical, magnetic, thermal, chemical, and biological properties. Therefore, they have received wide attention in the preparation of composite materials [3-5]. As a rare earth element, nano-cerium oxide particles are added as additives to the matrix to enhance the required properties, such as the hardness of the matrix, oxidation characteristics, and wear resistance [6]. Moreover, the unique electronic structure of nano-CeO<sub>2</sub> particles helps form a dense coating [7]. Wang et al. [8] showed that incorporating nano-CeO<sub>2</sub> particles into the coating can significantly increase its microhardness. Lei et al. [9] added a PANI/CeO<sub>2</sub> composite to a carbon steel coating, which can be used as a corrosion inhibitor, and thereby improved the corrosion resistance of the carbon steel epoxy coating tested in a 3.5% NaCl solution. However, in an electrodeposition process, the nanoparticles agglomerate, making the coating to exhibit a low and uneven nanoparticle content [10]. Therefore, the electrodeposition process needs to be modified. In addition to the conventional plating process parameters (current density, plating solution, temperature, and plating time), adding an external field, such as a magnetic field, could help regulate the electrodeposition process.

Magnetic field-assisted jet electrodeposition is an electrodeposition technology that has developed rapidly in recent years [11, 12]. In this technique, the interaction between electric and magnetic fields is utilized to significantly influence the co-deposition process of metal ions. Improving the deposition environment has an impact on surface morphologies and properties. [13, 14]. Peipmann et al. [15] found that the introduction of a vertical magnetic field during the preparation of an electrode nickel layer is beneficial for improving the current efficiency, and the content of the nano-alumina particles in the coating was significantly increased. Wang et al. [16] found that the addition of a magnetic field affects the preferred orientation of the nickel crystal phase. With the increase in the magnetic field strength, the promotion effect on Ni(220) was strengthened, and the grain growth on the Ni(200) crystal phase was inhibited. The influence of the vertical magnetic field on the mass transfer process is mainly the result of the magnetohydrodynamic (MHD) effect and the changes in the structure of the diffusion layer on the electrode surface [17]. Related scholars believe that the MHD effect reduces the thickness of the diffusion layer, thereby facilitating material transfer [18].

Based on the above analysis, we selected 45# steel as the metal substrate and applied jet electrodeposition under the assistance of a vertical magnetic field to prepare Ni-CeO<sub>2</sub> composite coatings. The effect of processing current density on the surface morphology of the composite coatings was then analyzed. Further, we studied their structure, composition, microhardness, and wear and corrosion resistances, so as to determine the best current density value for coating preparation.

## 2. EXPERIMENTAL

### 2.1. Sample preparation and electrodeposition

The test material was 45# steel (25 mm × 10 mm × 8 mm). Table 1 lists the compositions and the corresponding contents of the electroplating solution used. The chemicals used were all analytically pure and prepared with deionized water. The size of the nano-CeO<sub>2</sub> particles used in the experiment was

in the range of 10–30 nm, and their concentration in the plating solution was 10 g/L. The cathode workpieces were polished with 800<sup>#</sup> and 1500<sup>#</sup> water sandpaper, successively. They were then pretreated before the jet electrodeposition—electro-clean degreasing → weak activation → strong activation—and rinsed with deionized water after each step. The pre-processed workpieces were placed in a jet electrodeposition test device for a jet coating test. During the jet electrodeposition process, the pH of the plating solution was in the range of 1.0–1.5, the magnetic induction intensity of the vertical magnetic field was 0.5 T, and the plating solution was maintained at a constant temperature of 60 °C. The processing was performed at current densities of 10, 15, 20, 25, and 30 A/dm<sup>2</sup>, and the plating time for each workpiece was 25 min. After the jet electrodeposition processing was completed, the workpieces were subjected to ultrasonic cleaning and drying treatment. Finally, their performances were evaluated.

**Table 1** Composition of plating solution

Plating solution composition	Content (g/L)
NiSO <sub>4</sub> ·6H <sub>2</sub> O	240
NiCl <sub>2</sub> ·6H <sub>2</sub> O	40
H <sub>3</sub> BO <sub>3</sub>	30
C <sub>6</sub> H <sub>8</sub> O <sub>7</sub>	10
CH <sub>4</sub> N <sub>2</sub> S	0.01
C <sub>12</sub> H <sub>25</sub> SO <sub>4</sub> Na	0.08
CeO <sub>2</sub>	10

## 2.2. Sample characterization

A scanning electron microscope (FEI–SEM, Quanta FEG250; FE Instruments, Oregon, USA) was used to observe the surface morphology of the coating. An energy dispersive X-ray spectroscopy (EDS) spectrum analyzer (XFlash 5030 Bruker AXS, Inc., Berlin, Germany) was used to determine the chemical composition of the coating in the line scanning and plane scanning modes (1 mm<sup>2</sup>). The phase structure of the coating was analyzed using an X-ray diffractometer (PANalytical X<sup>pert</sup>; PANalytical Inc.) at an operating voltage of 40 kV, scan rate of 5 °/min, and scanning range of 20–90° to determine the phase structure. A microhardness measuring instrument (Duramin-40; Struers Inc., Denmark) was used to measure the microhardness of the composite coating surface. When testing, a GCr15 grinding ball with a diameter of 4 mm was selected, and the grinding ball was loaded onto the surface of the composite coating. The following parameters were set: Linear reciprocating friction for 20 min, reciprocating speed of 500 T/min, wear scar length of 4 mm, and test load of 320 g. Subsequently, five measurements were made, and the average value was taken as the measurement result. A wear test was carried out on a CFT-I material surface performance comprehensive tester. During the detection, the GCr15 grinding ball with a diameter of 4 mm was scratched back and forth on the coating surface for 20 min; the load was 320 g, and the scratch length was 4 m. An OLYMPUSLEXT4100 laser confocal microscope (Japan Olympus Company) was used to measure the dimensional parameters of the scratches on the coating surface. An electrochemical workstation (CS350; Wuhan Corrtest Instruments Corp.,

Ltd., China) was used to study the corrosion resistance of the composite coating. The test workpiece was immersed in a 3.5 wt.% NaCl solution, and a dynamic potential scan (a scan rate of 1 mV/s) method was applied to obtain the polarization curve of the coatings. Subsequently, the epitaxy method was applied to determine the parameters that characterize the corrosion resistance, self-corrosion potential, and self-corrosion current. The electrochemical impedance spectroscopy (EIS) was used to measure the impedance spectrum of the coating in the corrosive medium at the open circuit potential. The test frequency range was  $10^{-2}$ – $10^{-5}$  Hz, swept from high to low. The ZSimpWin software was used to fit and analyze the obtained impedance spectrum.

### 3. RESULTS AND DISCUSSION

#### 3.1. Electrodeposition mechanism

Figure 1 shows the schematic of the co-deposition process of Ni and CeO<sub>2</sub> on the substrate surface. This process mainly includes two stages: a nucleation stage and a growth stage.

The nucleation stage: The Ni ions and nano-CeO<sub>2</sub> particles move to the surface of the cathode matrix under the action of an external electric field. Under the actions of the external electric field and a vertical magnetic field, the ions are subjected to an electric field force and a Lorentz force, respectively. This changes their trajectory, and the ions follow the direction of spiral diffusion [19, 20]. Moreover, owing to the MHD effect, the agglomeration phenomenon of the nano-CeO<sub>2</sub> particles is weakened. The nano-CeO<sub>2</sub> particles are regularly adsorbed on the workpiece. Because of their high surface energy, they form nucleation sites on the coating surface. The magnetic field helps mechanically stir the plating solution, which is beneficial to the uniform distribution of the particles on the surface of the plating layer [21].

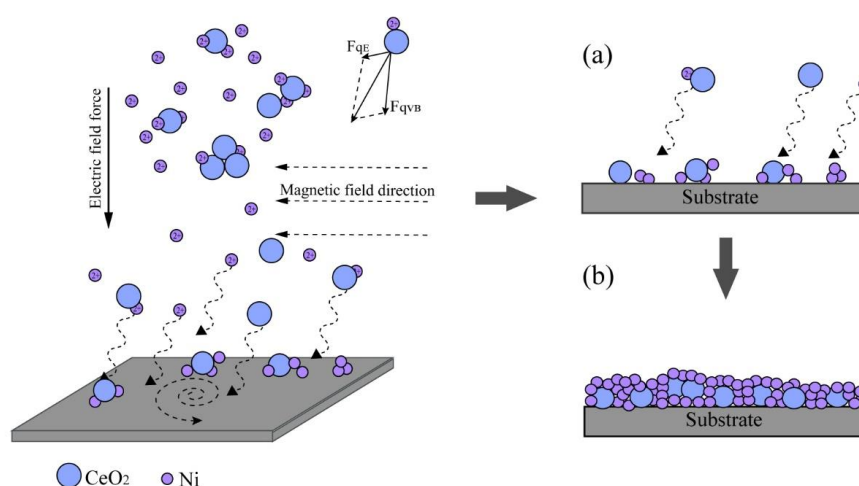


**Figure 1.** Growth mechanism of Ni–CeO<sub>2</sub> composite coating prepared by jet electrodeposition with the assistance of a magnetic field

The grain growth stage: With the increase in the plating time, the Ni<sup>2+</sup> ions are attracted by the cathode potential and are continuously transferred to the surface of the workpiece. A reduction reaction

occurs on the workpiece surface and continues along the nucleation sites of the Ni crystal grains. Thus, the thickness of the coating increases.

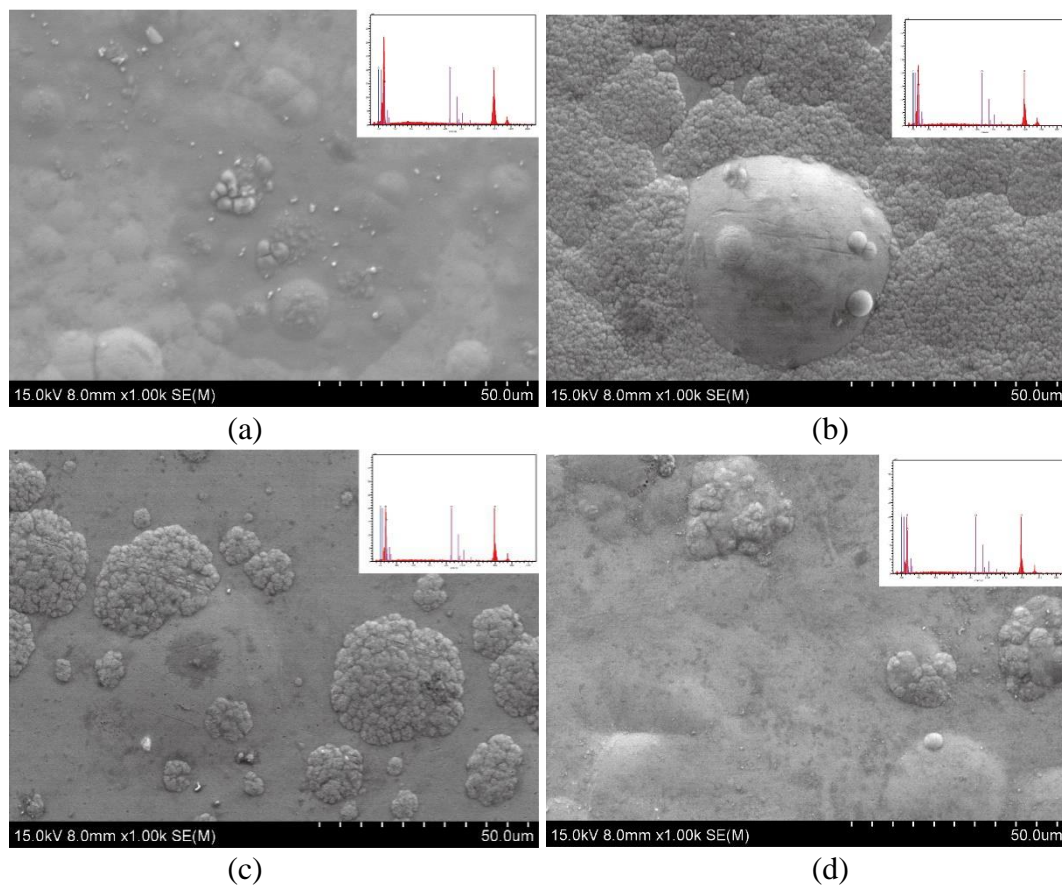
### 3.2. Surface morphologies

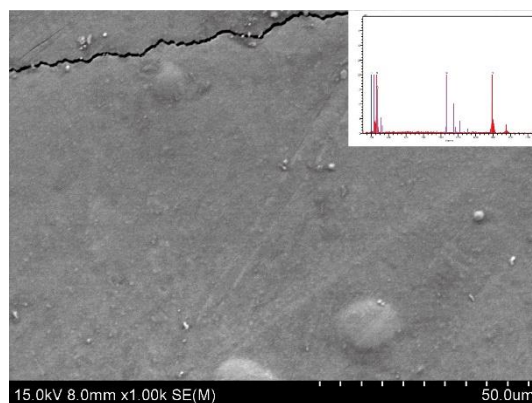
Figure 2 shows the surface morphologies of the Ni–CeO<sub>2</sub> composite coatings prepared using the magnetic field-assisted jet electrodeposition under different current densities. As shown, the nano-CeO<sub>2</sub> particles are evenly distributed on the coating surface, mainly concentrated at the cell boundary of the matrix metal. Moreover, the coating surface contains cracks. The combination of hard nanoparticles and the matrix metal causes a dispersion of the matrix metal [22]. The introduction of the vertical magnetic field produces the MHD effect, which is equivalent to scouring the surface of the cathode, thus promoting the elimination of the hydrogen generated by the hydrogen evolution reaction at the cathode and thereby reducing the defects on the coating surface [23].

When the current density is low (Figure 2(a)), the cell structure of the coating surface is not evident, and particles are attached onto the coating surface. This is because at low current densities, the deposition rate of the ions is low, the nucleation rate of the crystal grains and the formation rate of the nucleation sites are both low, and the coating is thin. The nano-CeO<sub>2</sub> particles easily agglomerate because of their high surface energy, and the low current efficiency makes it difficult to make the nano-CeO<sub>2</sub> particles to uniformly distribute on the coating surface, and the flatness of the coating is poor. When the current density increases to 15 A/dm<sup>2</sup> (Figure 2(b)), the spherical unit cells form clusters, the particle size is small, the size is relatively uniform, and the coating is relatively flat and dense, without any evident cracks. This is because of the high current density, which increases the current efficiency and accelerates the movement of the ions to the cathode. The introduction of the vertical magnetic field reduces the agglomeration of the nano-CeO<sub>2</sub> particles and promotes the entry of nano-CeO<sub>2</sub> particles into the coating, thus increasing the number of nucleation sites of the crystal grains, and the crystal grains are refined. The refined grains increase the grain boundaries of the matrix. The dislocation movement between the coating and the substrate and the expansion of the microcracks are hindered, the coating is strengthened, and the compactness of the coating is improved [24]. When the current density increases to 20 A/dm<sup>2</sup> (Figure 2(c)), the number of spherical unit cell clusters on the coating surface decreases, the cell structure boundary is blurred, and the flatness of the coating surface is significantly improved. The high current density improves the current efficiency, the speed at which the Ni<sup>2+</sup> ions move to the vicinity of the cathode is accelerated, the coating continues to grow epitaxially, the grain growth speed is increased, and the coating becomes thicker. In addition, the magnetic fluid effect (MHD) produced by the magnetic field has a refining effect on the grains in the coating and a modification effect on the grain morphology. The surface roughness of the coating is reduced, the current is evenly distributed, the tip effect is avoided, and a compact coating is obtained. When the current density is 25 A/dm<sup>2</sup> (Figure 2(d)), the cell structure boundary on the coating surface is relatively clear; however, the cell structure varies in terms of the size and height. This is because an increase in the current density accelerates ion deposition, and the increase in the grain growth speed increases the coating thickness. Under the action of the vertical magnetic field, the grain growth gradually transforms from an epitaxial growth state to a free growth

state, resulting in an uneven coating thickness and reduced flatness of the coating. When the current density continues to increase to  $30 \text{ A/dm}^2$  (Figure 2(e)), the uniformity of the coating surface is improved, and the particles are attached; however, there are cracks. This is because at higher current densities, the coating grows freely, and the thickness increases; the activity of the cathode hydrogen evolution reaction is enhanced, and the large amount of hydrogen generated adversely affects the regular ordering of the nano- $\text{CeO}_2$  particles. As the current density increases, the metal discharge speed is accelerated, the number of particles entering the coating decreases, and the accelerated Ni deposition rate will ensure that the adsorbed nanoparticles on the coating surface are covered. This leads to a thick coating and local internal stress concentration [25], which cause cracks on the coating surface.

The MHD effect produced by the vertical magnetic field is beneficial to the mass transfer process. The ions controlled by the mass transfer process in the electrodeposition are most significantly affected by the magnetic field. Typically, the hydrogen atom reduction process is affected by the mass transfer in the electrodeposition process, so the addition of a vertical magnetic field is conducive to the precipitation of hydrogen ions, thereby reducing the adverse effect of hydrogen on the coating surface. As the current density increases, the compactness and flatness of the surface morphology of the Ni– $\text{CeO}_2$  composite coating are improved, and the coating thickness is increased accordingly. When the current density is  $20 \text{ A/dm}^2$ , the Ni– $\text{CeO}_2$  composite coating prepared by the magnetic field-assisted jet electrodeposition has the best surface morphology and compactness, and there are few impurities on its surface. An excessive current density is not conducive to the surface performance of the coating.





(e)

**Figure 2.** Surface morphologies of Ni–CeO<sub>2</sub> composite coatings prepared under varying current density: (a) 10 A/dm<sup>2</sup>, (b) 15 A/dm<sup>2</sup>, (c) 20 A/dm<sup>2</sup>, (d) 25 A/dm<sup>2</sup>, (e) 30 A/dm<sup>2</sup>

### 3.3. XRD and EDS analysis

Figure 3 shows the XRD diffraction patterns of the Ni–CeO<sub>2</sub> composite coatings prepared by jet electrodeposition under a vertical magnetic field. As shown, the coating structure is amorphous. This is because the vertical magnetic field increases the content of nano-CeO<sub>2</sub> particles added to the coating, which is beneficial to the formation of amorphization [26]. The figure clearly shows a strong peak of Ni(111) and a relatively strong peak of Ni(200), in addition to the weak peak of Ni(220). Due to the low concentration of the nano-CeO<sub>2</sub> particles, the Ce content in the coating is relatively low compared with the Ni element. Therefore, no evident Ce peak can be seen in the XRD pattern.

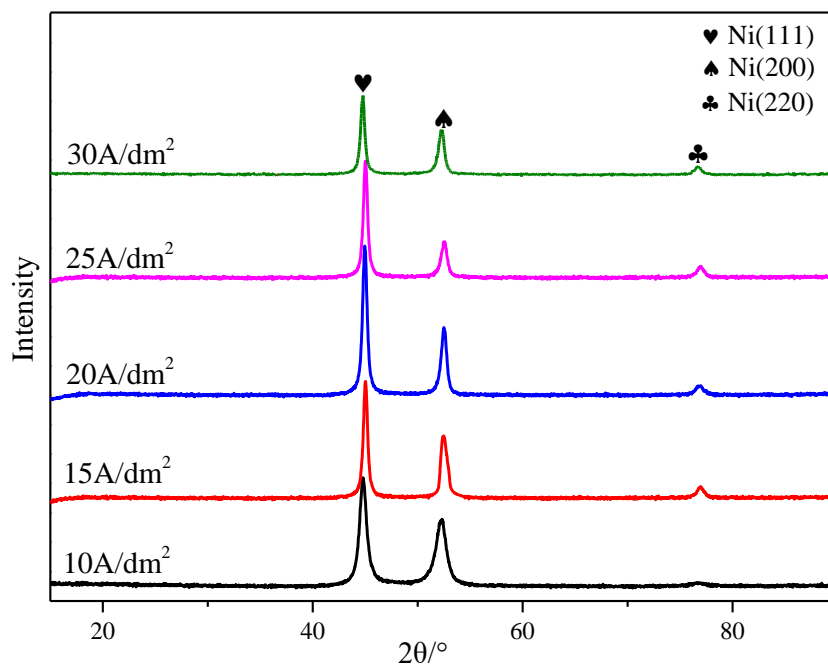
The figure shows main peaks of Ni(111) and Ni(200) crystal phases in the  $2\theta$  range of 40–60° and weak peaks of Ni(220) in the  $2\theta$  range of 70–80°. With the increase in the current density, the Ni crystal phase transformation to Ni(111) is evident. When the current density is low (10 A/dm<sup>2</sup>), the crystal plane orientation of the composite coating is stronger than the Ni(111) and Ni(200) crystal orientations, and the peak intensity of Ni(220) is extremely low. When the current density increases to 15 A/dm<sup>2</sup>, the Ni(200) crystal phase gradually transforms to Ni(111). At the same time, a weak peak of Ni(220) orientation can be seen at  $2\theta = 76^\circ$ . When the current density is 20 A/dm<sup>2</sup>, the strengths of the Ni(200) and Ni(111) crystal phases are weakened, and the weak peak of Ni(220) tends to increase evidently. When the current density continues to increase to 25–30 A/dm<sup>2</sup>, the intensities of the three Ni crystal phase peaks decrease. The reasons are as follows: (1) After applying a vertical magnetic field, the free energy of the plating solution system increases, and more adsorbed atoms transition to a stable state. The high-energy Ni(200) migrates to the low-energy crystal plane, so the proportion of Ni(200) crystal planes decreases [27]. (2) After the vertical magnetic field is applied, the MHD effect is generated on the cathode surface, which promotes the transfer of the hydrogen ions, increases the concentration of the hydrogen ions on the cathode surface, and reduces the pH, which facilitates the preferential orientation of the Ni(111) crystal planes. (3) As the current density increases, the reduction reaction accelerates near the cathode, and the metal atoms on the cathode surface have no time to diffuse to the most stable state, i.e., the diffusion channels are occupied by the subsequently reduced atoms, thereby

hindering their further diffusion, leading to the electrodeposition of Ni(200). The proportion of crystal planes increases, making them preferentially oriented.

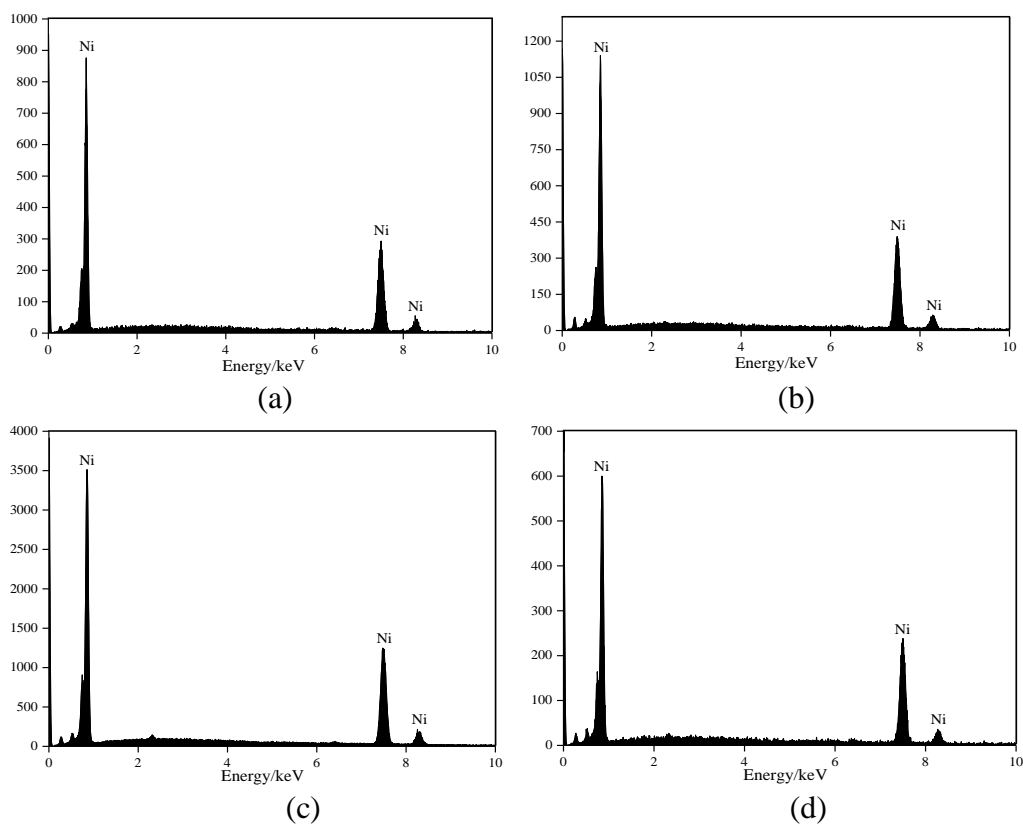
The average sizes of the average Ni grains in the coating calculated using the Scherrer formula [28] are 16.7, 16.5, 9.3, 16.8, and 17.9 nm, respectively. Thus, we can confirm that the prepared coating is an Ni–CeO<sub>2</sub> nanocomposite coating. The smaller the grain size, the better the compactness of the composite coating. This is because the MHD effect generated by the magnetic field can break up the crystal nuclei generated on the substrate surface, and then generate new, finer, and smaller crystal nuclei, so that the grain size at the coating surface is smaller and more uniform, i.e., fine crystal strengthening.

Figure 4 and Table 2 show the EDS surface scanning energy spectra of the coatings and the proportion of the surface atom content in the coatings, respectively. The Ni–CeO<sub>2</sub> composite coatings prepared by jet electrodeposition with the aid of the magnetic field contain large amounts of Ni and O elements. With the increase in the current density, the atomic content of Ce element increases. Under the assistance of the magnetic field and when the current density is 20 A/dm<sup>2</sup>, the Ni element content on the coating surface is the highest, 94.3 at.%. When the current density increases to 25 A/dm<sup>2</sup>, the atomic content percentage of the Ce element on the coating surface is at most 2.45 at.%. This can be attributed to the MHD effect produced by the magnetic field and the influence of the magnetic field on the electron transfer process when the magnetic field-assisted jet electrodeposition is used to prepare the Ni–CeO<sub>2</sub> composite coating. These two effects facilitate the movement of the nano-CeO<sub>2</sub> particles and metal Ni ions toward the cathode; thus, the nano-CeO<sub>2</sub> particles are more likely to enter the coating. The MHD effect will cause the plating solution to flow and increase the mass transfer process of the reactant material to the cathode. The high current density effectively alleviates the adverse effects of hydrogen precipitation at the cathode surface on the ion deposition process [29]. At high current densities, the hydrogen precipitated at the cathode surface is removed in time, and the deposition rate of the Ni ions increases, thus prompting the nano-cerium oxide particles to enter the coating. The addition of the vertical magnetic field accelerates the electrodeposition process, increases the current density, facilitates the entry of nano-CeO<sub>2</sub> particles into the coating, and increases the contents of the various elements in the coating.

The EDS chart shows that the Ni content in the coating increases with an increase in the current density. When the current density is 20 A/dm<sup>2</sup>, the atomic content of Ni in the coating is 94.3 at.%, and the atomic content of Ce is 2.13 at.%. When the current density is 25 A/dm<sup>2</sup>, the maximum of Ce is 2.45 at.%. The introduction of the magnetic field makes the particles in the coating more uniformly distributed. The high current density facilitates the entry of the nanoparticles and Ni elements into the coating, thereby increasing the contents of Ni and Ce elements.



**Figure 3.** XRD spectra of the Ni–CeO<sub>2</sub> composite coatings as a function of the current density



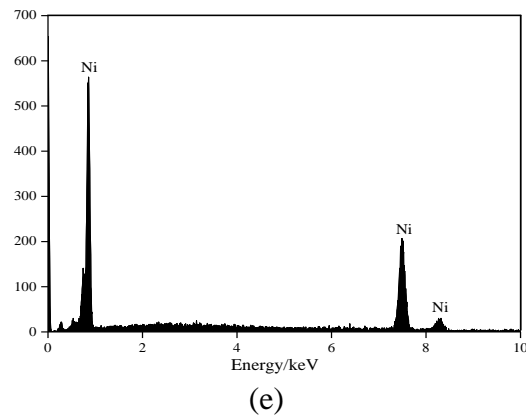


**Figure 4.** Energy dispersive spectroscopy (EDS) analysis of Ni–CeO<sub>2</sub> composite coatings prepared at current densities of: (a) 10 A/dm<sup>2</sup>, (b) 15 A/dm<sup>2</sup>, (c) 20 A/dm<sup>2</sup>, (d) 25 A/dm<sup>2</sup>, (e) 30 A/dm<sup>2</sup>

**Table 2.** Elemental chemical composition (at.%) of Ni–CeO<sub>2</sub> composite coatings obtained by EDS

	10 A/dm <sup>2</sup>	15 A/dm <sup>2</sup>	20 A/dm <sup>2</sup>	25 A/dm <sup>2</sup>	30 A/dm <sup>2</sup>
Ni (at.%)	94.75	93.81	94.3	92.58	93.36
Ce (at.%)	0.81	2.08	2.13	2.45	2.14
O (at.%)	4.45	4.11	4.45	3.56	4.15

### 3.4. Microhardness

A microhardness test was carried out on the Ni–CeO<sub>2</sub> composite coating samples prepared using the magnetic field-assisted jet electrodeposition. Figure 5 shows the results obtained. As shown, the microhardness of the Ni–CeO<sub>2</sub> composite coating first increases and then decreases with the change in the processing current density. The factors affecting the microhardness of the composite coating include the matrix metal, the nature of the added particles, and the number and size of the hard phases [30, 31]. Hans Ferik [32] showed that adding nano-CeO<sub>2</sub> particles into a plating solution significantly increases the microhardness of the composite coating.

At a low current density (10 A/dm<sup>2</sup>), the microhardness of the composite coating is low, only 597.08 HV<sub>0.1</sub>. At low current densities, the deposition rate of the ions is lower, the coating is thinner, and the hardness value is lower. When the current density increases to 15 A/dm<sup>2</sup>, the microhardness of the composite coating is 621.6 HV<sub>0.1</sub>, the microstructure hardness of the composite coating has been improved. When the current density is 20 A/dm<sup>2</sup>, the microhardness of the composite coating is the highest, 665.78 HV<sub>0.1</sub>, which is 11.5% higher than that of the composite coating prepared under a current density of 10 A/dm<sup>2</sup>. This is because under the action of a vertical magnetic field, the nano-CeO<sub>2</sub> particles are uniformly distributed in the coating. With the increase in the current density, the number of nano-CeO<sub>2</sub> particles entering the coating increases under the attraction of the cathode potential, which increases the metal content on the cathode surface. At the nucleation sites, the ion deposition rate is accelerated, the thickness of the coating increases, and the hardness value increases; however, when the

current density continues to increase to 25 A/dm<sup>2</sup>, the microhardness of the composite coating decreases to 614.28 HV<sub>0.1</sub>. When the current density reaches 30 A/dm<sup>2</sup>, the microhardness is reduced to a minimum of 544.28 HV<sub>0.1</sub>. This is because when the current density is too high, the current density at the cathode increases, the overpotential of the cathode will also increase correspondingly, the electric field force increases, and the electrostatic attraction of the cathode to the nano-cerium oxide particles that adsorb the Ni<sup>2+</sup> increases, thereby promoting the Co-deposition process of the nano-cerium oxide particles and Ni ions. However, when the current density is too high, the exchange current of the Ni ions is greater than that of the nano-cerium oxide particles, which has an adverse effect on Ni–CeO<sub>2</sub> co-deposition.

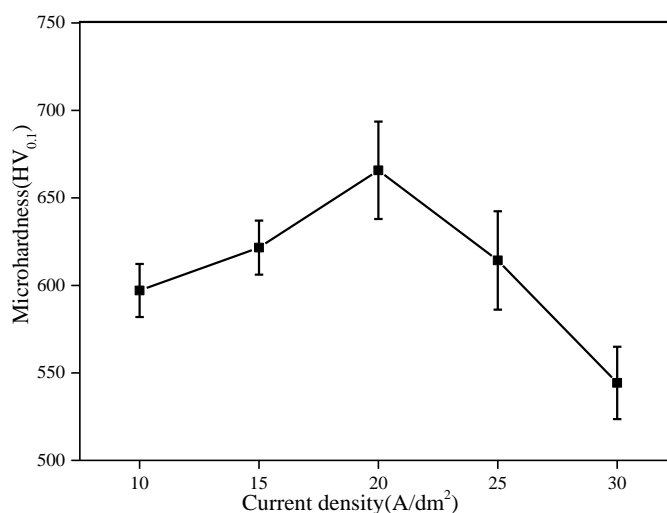


**Figure 5.** Microhardness of Ni–CeO<sub>2</sub> composite coating

### 3.5. Wear resistance

Figure 6 shows the surface appearance of the composite coating observed under an electron microscope after being polished by a grinding ball for 20 min. The wear scar interface in Figure 6(a) has a large coating shedding area. The wear mechanism is surface fatigue wear. The surface of the coating and the grinding ball form a friction pair. Oxidative wear and adhesive wear appear. As the wear time increases, the coating surface exhibits fatigue wear under the cyclic stress. This makes the coating surface to peel off due to fatigue [33]. Because the coating is thinner at a low current density, the wear resistance is poor, and the coating wear is serious. An EDS line scan is performed on the wear interface, and the results show that the coating changes after being rubbed by the grinding ball. The composite coating prepared at 10 A/dm<sup>2</sup> exhibits large fluctuations in the atomic content percentages of Ni and Fe at the wear interface. The atomic content of Ni decreases sharply, whereas that of the Fe increases. The increased Fe content comes from the substrate. Evidently, the coating has undergone significant wear because of the low current density, low ion deposition rate, slow grain growth, thin coating, and poor wear resistance. The surface of the wear scar shown in Figure 6(b) has a clear gully, and wear debris is attached to the surface, mainly due to adhesive wear, and the adhesion node between the coating surface

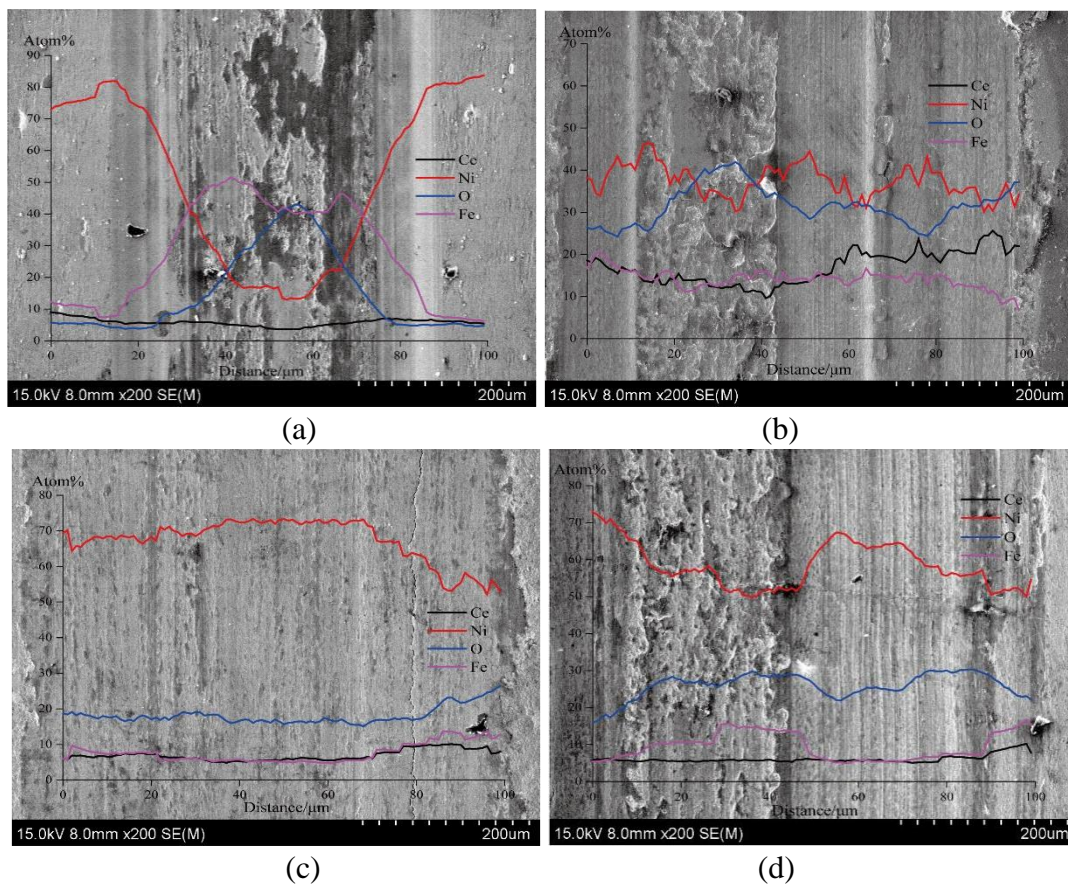
and the grinding ball is broken [34]. As the current density increases, the coating thickness increases, and the wear resistance of the composite coating prepared at a current density of 10 A/dm<sup>2</sup> is improved. Combined with the EDS line scan results, the composite coating prepared at a current density of 25 A/dm<sup>2</sup> exhibits a significant increase in the O element content at the wear scar, indicating that the coating underwent oxidative wear during the wear process [35], the coating will cause the wear debris to fall off during the wear of the grinding ball, and the new surface will be. The friction pair continues to slide relative to each other, forming oxidation products, which alternate between adhesive wear and oxidative wear. The wear scar interface shown in Figure 6(c) is relatively flat, with fewer side-by-side furrows, abrasive wear [36], and a crack. In the EDS line scan results of the composite coating prepared at a current density of 20 A/dm<sup>2</sup>, the content of each element is relatively stable without evident fluctuations, indicating that the composite coating surface is less damaged by abrasion and that the coating has a good wear protection performance. The wear mechanism shown in Figure 6(d) is adhesive wear and abrasive wear. On the left side of the wear interface, the sliding of the grinding ball relative to the workpiece produces wear debris. The fallen wear debris moves between the friction pairs, thereby further abrading the coating surface. A large number of neatly arranged furrows can be observed at the wear scar interface. This can be attributed to the relative sliding friction between the grinding ball and the workpiece surface. The wear debris on the coating surface wears the coating surface again, resulting in “microcutting” [37], indicating that the wear resistance of the coating is reduced at this time. The wear on the left side of the wear scar interface of the coating prepared at a current density of 25 A/dm<sup>2</sup> is more serious. The Ni element content is somewhat reduced, whereas the contents of Fe and O elements increase. There are damages on the coating surface. The increased Fe element content comes from the matrix, and the O element content comes from the oxidative wear. With the increase in the current density, the wear resistance of the coating is not always improved. Figure 6(e) shows small pieces of grinding-off areas at the wear interface and a large number of wear scars at the center. The furrows due to the abrasive wear are deep and shallow. In the line scan results of the Ni–CeO<sub>2</sub> composite coating prepared at a current density of 30 A/dm<sup>2</sup>, the atomic percentage of Ni is decreased, and the O element is increased overall, indicating that there is always oxidative wear during wear and that the Ni element in the coating is exposed, producing NiO and other oxides in the air. The wear resistance of the coating is poor, indicating that the excessive current density is not conducive to the wear resistance of the coating.

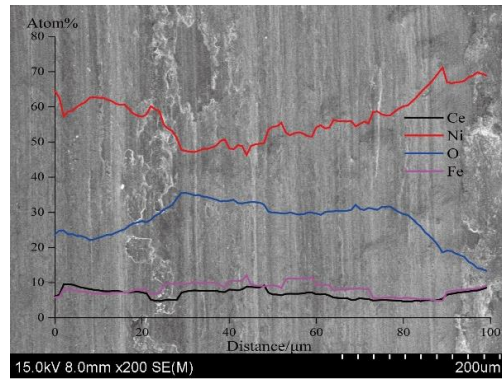
Figure 7 shows the wear scar interface of the Ni–CeO<sub>2</sub> composite coating captured under a confocal laser microscope. Table 3 lists a series of parameter values related to the wear scar interface. Combined with Figure 7 and Table 3, we find that, with the increase in the current density, the parameter values related to the wear scars first decrease and then increase. Generally, under the same wear conditions, the smaller the width of the wear, the smaller the depth of the wear section, and the smaller the area of the wear section, the better the wear resistance of the coating.

The wear section of the composite coating prepared under a current density of 10 A/dm<sup>2</sup> has a width of 693 μm, a height of 13 μm, and a cross-sectional area of 12389 μm<sup>2</sup>. At low current densities, due to the low grain nucleation rate and grain growth rate, the coating is thin and poor wear-resistant performance. The wear section width of the composite coating prepared under a current density of 15 A/dm<sup>2</sup> is 650 μm, the height is 12 μm, and the cross-sectional area is 11850 μm<sup>2</sup>. Compared with the coating prepared under a coating density of 10 A/dm<sup>2</sup>, the coating wear resistance performance is

improved, the current density is increased, and the ion growth rate increases. The ions are subjected to the Lorentz force under the action of the vertical magnetic field and are uniformly distributed on the coating surface, the thickness of the coating increases uniformly, and the wear resistance is improved. The width, height, and cross-sectional area of the composite coating prepared under a current density of 20 A/dm<sup>2</sup> are the lowest, respectively, 630 μm, 11 μm, and 11720 μm<sup>2</sup>. In comparison, the cross-sectional parameter value of the composite coating prepared under a current density of 25 A/dm<sup>2</sup> increases, with a width of 682 μm, a height of 14 μm, and a cross-sectional area of 13586 μm<sup>2</sup>. When the current density reaches 30 A/dm<sup>2</sup>, the width, height, and cross-sectional area of the wear scar cross-section increase to 681 μm, 13 μm, and 13742 μm<sup>2</sup>, respectively.

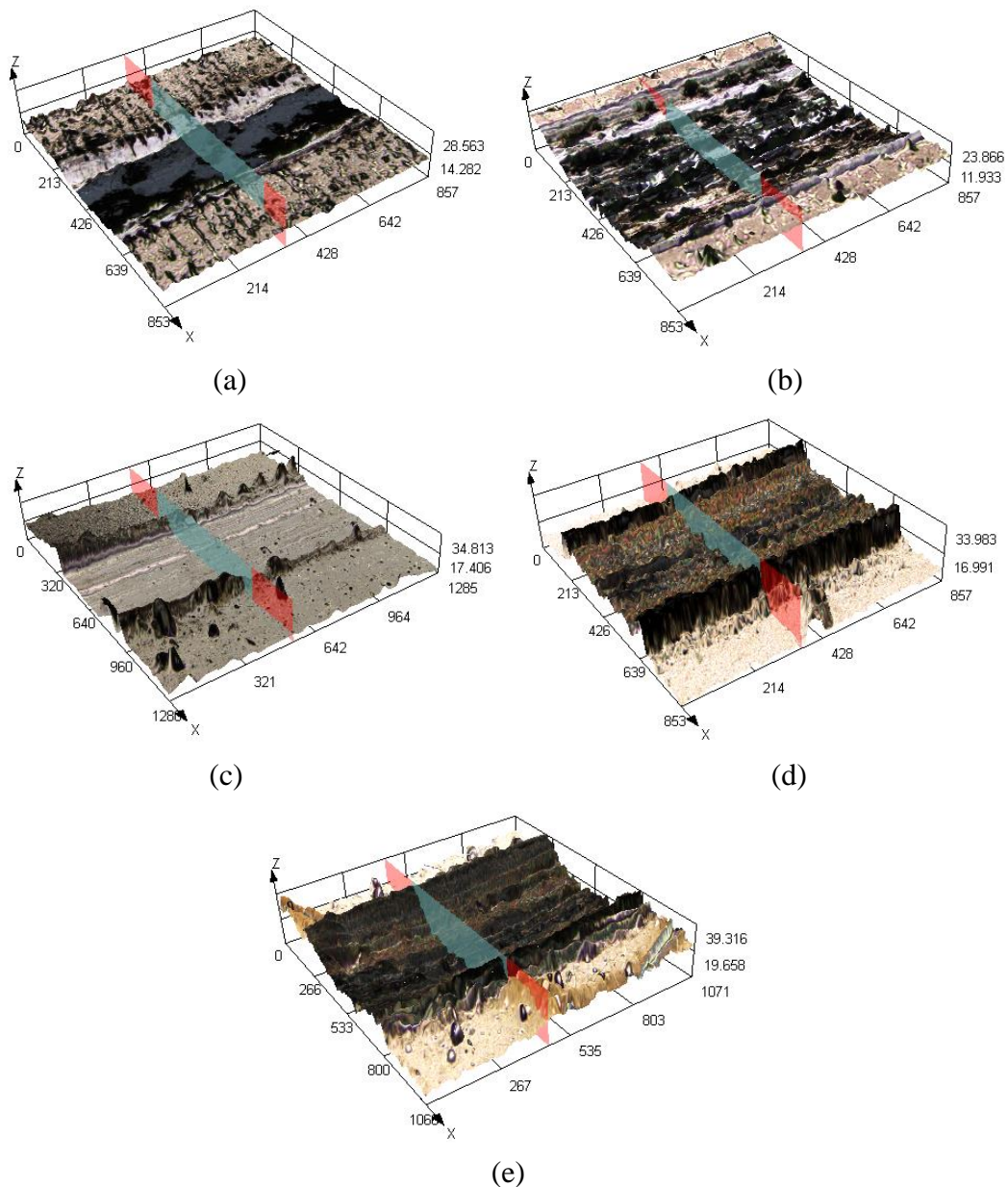
Combining the wear interface morphology and wear section parameter values, we find that the microhardness of the coating is lower, and the wear resistance is poor at low current densities. The increase in the current density optimizes the wear resistance of the coating. The composite coating prepared at a current density of 20 A/dm<sup>2</sup> has the highest microhardness and the best wear resistance. However, when the current density is too high, the microscopicity of the composite coating decreases, and the wear resistance will decrease accordingly.





(e)

**Figure 6.** Surface morphologies of wear marks in the coating prepared at current densities of: (a) 10 A/dm<sup>2</sup>, (b) 15 A/dm<sup>2</sup>, (c) 20 A/dm<sup>2</sup>, (d) 25 A/dm<sup>2</sup>, (e) 30 A/dm<sup>2</sup>



(e)

**Figure 7.** Outlines of wear interfaces of coatings prepared at various current densities: (a) 10 A/dm<sup>2</sup>, (b) 15 A/dm<sup>2</sup>, (c) 20 A/dm<sup>2</sup>, (d) 25 A/dm<sup>2</sup>, (e) 30 A/dm<sup>2</sup>

**Table 3.** Parameters of wear mark section

Current density for coating preparation (A/dm <sup>2</sup> )	Width (μm)	Height (μm)	Scratch area (μm <sup>2</sup> )
10	693	13	12389
15	650	12	11850
20	630	11	11720
25	682	14	13586
30	681	13	13742

### 3.6. Corrosion resistance of Ni–CeO<sub>2</sub> composite coatings

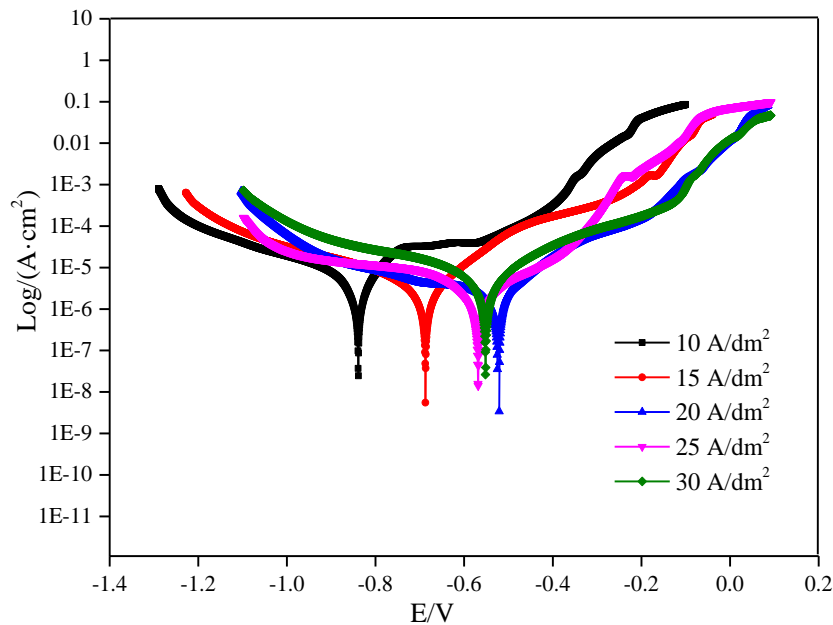
#### 3.6.1. Potentiodynamic polarization curve

Figure 8 shows the polarization potential curves of the composite coatings prepared using magnetic field-assisted electrodeposition at different current densities. Table 4 lists the parameter values at the open circuit potential during the corrosion process. Related research results show that, the lower the self-corrosion current at the self-corrosion potential and the more positive the self-corrosion voltage, the better the corrosion protection performance of the coated workpiece. Moreover, the coating is less likely to undergo oxidation–reduction reactions owing to the formation of a passivation film on the coating surface. This film hinders the contact between the metal and the corrosive medium and improves the corrosion resistance of the coating [38, 39].

With the help of the CorrTest software and polarization curve epitaxy, the self-corrosion current  $I_{corr}$ , self-corrosion voltage  $E_{corr}$ , and corrosion rate in the corrosion circuit are obtained.  $B_a$  and  $B_c$  in Table 4 denote the anodic and cathodic dynamic polarization potential slopes, respectively. Figure 8 shows that the self-corrosion potential first increases and then decreases with the increase in the current density, and the self-corrosion current and corrosion efficiency both decrease first and then increase accordingly. When the current density is 10 A/dm<sup>2</sup>, the self-corrosion current of the composite coating is  $6.3235 \times 10^{-7}$  A·cm<sup>-2</sup>, the self-corrosion voltage is -0.833 V, and the corrosion rate of the workpiece is  $7.6537 \times 10^{-1}$  mm/a, which shows that the composite coating has a poor corrosion resistance. When the current density is 15 A/dm<sup>2</sup>, the self-corrosion current is  $5.7115 \times 10^{-7}$  A·cm<sup>-2</sup>, and the self-corrosion voltage is -0.621 V. The self-corrosion performance of the composite coating has been improved. The corrosion rate of the workpiece in the corrosive medium is  $6.9129 \times 10^{-2}$  mm/a. Compared with the corrosion resistance of the coating prepared under a current density of 10 A/dm<sup>2</sup>, the corrosion resistance is improved. When the current density is 20 A/dm<sup>2</sup>, the self-corrosion current is reduced to a minimum value of  $2.0274 \times 10^{-7}$  A·cm<sup>-2</sup>, and the self-corrosion potential reaches the maximum value of -0.553V at this time. The corrosion rate is the lowest  $2.4538 \times 10^{-3}$  mm/a, and the corrosion resistance of the coating is the best. When the current density increases to 25 A/dm<sup>2</sup>, the self-corrosion current increases to  $6.0367 \times 10^{-6}$  A·cm<sup>-2</sup>, the negative offset of the self-corrosion potential is -0.597 V, the rate of corrosion of the workpiece at this time is  $7.3065 \times 10^{-2}$  mm/a, and the corrosion resistance of the coating decreases. When the current density continues to increase to 30 A/dm<sup>2</sup>, the self-corrosion current

increases to  $8.5813 \times 10^{-6} \text{ A} \cdot \text{cm}^{-2}$ , the self-corrosion voltage decreases to  $-0.551 \text{ V}$ , the corrosion rate increases to  $1.0386 \times 10^{-1} \text{ mm/a}$ , and the corrosion resistance of the composite coating decreases.

In summary, the self-corrosion current of the composite coating prepared at a current density of  $20 \text{ A/dm}^2$  is the lowest, the self-corrosion voltage is the highest, and the corrosion protection performance of the substrate is excellent.



**Figure 8.** Potentiodynamic polarization curves of Ni–CeO<sub>2</sub> composite coatings prepared by jet electrodeposition with the assistance of a magnetic field

**Table 4.** Corrosion electrochemical parameters of Ni–CeO<sub>2</sub> composite coatings prepared by jet electrodeposition with the assistance of a magnetic field

Current density for coating preparation (A/dm <sup>2</sup> )	B <sub>a</sub> (mV)	B <sub>c</sub> (mV)	I <sub>corr</sub> (A·cm <sup>-2</sup> )	E <sub>corr</sub> (V)	Corrosion rate (mm/a)
10	175	85	$6.3235 \times 10^{-7}$	-0.833	$7.6537 \times 10^{-1}$
15	158	154	$5.7115 \times 10^{-7}$	-0.621	$6.9129 \times 10^{-2}$
20	136	179	$2.0274 \times 10^{-7}$	-0.553	$2.4538 \times 10^{-3}$
25	210	414	$6.0367 \times 10^{-6}$	-0.597	$7.3065 \times 10^{-2}$
30	237	427	$8.5813 \times 10^{-6}$	-0.551	$1.0386 \times 10^{-1}$

### 3.6.2. EIS measurements

The EIS was used to explore the corrosion protection behavior of the composite coating in a 3.5% NaCl solution. Figure 9 and Table 5 present the Nyquist diagrams of the AC impedance testing at different scanning frequencies and the parameter values obtained after simulation with the equivalent circuit. The figure shows that the capacitance impedance spectrum of the composite coating is arc-

shaped. The larger the radius of the arc, the greater the charge transfer resistance and the better the corrosion resistance [40]. The ZView software was used to perform equivalent fitting of the AC impedance map. Figure 10 shows the equivalent circuit diagram of the software used to simulate the AC impedance map of the Ni–CeO<sub>2</sub> nanocomposite coating. In the figure, R<sub>s</sub> is the solution resistance, R<sub>p</sub> is the charge transfer resistance of the coating, CPE is the constant phase element, and the impedance is

$$Z = \frac{1}{Y_0(j\omega)^{-n}}$$

Here, there are two parameters: the constant  $Y_0$ , whose dimension is  $\Omega^{-1}\cdot\text{cm}^{-2}\cdot\text{s}^{-n}$ , and the parameter  $n$ , which is a dimensionless index. When  $n = 0$ , the CPE element is a pure resistor; when  $n = 1$ , the CPE is an ideal capacitor. In the actual solution,  $n$  is between 0 and 1 [41].

The arc radius of the capacitive impedance of the composite coating increases first and then decreases with the increase in the current density. When the current density is 10 A/dm<sup>2</sup>, the composite coating exhibits a low capacitive impedance, a charge transfer resistance of 587  $\Omega\cdot\text{cm}^{-2}$ , and the worst corrosion protection performance. When the current density increases to 15 A/dm<sup>2</sup>, the capacitive impedance of the composite coating increases accordingly, and the charge transfer resistance at this time is 1556  $\Omega\cdot\text{cm}^{-2}$ , which represents an improvement in the corrosion protection performance of the coating. When the current density increases to 20 A/dm<sup>2</sup>, the composite coating exhibits the highest capacitive impedance arc radius and charge transfer resistance (2467  $\Omega\cdot\text{cm}^{-2}$ ). At this time, the composite coating provides the best corrosion protection performance for the substrate. When the current density reaches 25 A/dm<sup>2</sup>, the capacitive impedance radius of the composite coating decreases, the charge transfer resistance decreases to 2120  $\Omega\cdot\text{cm}^{-2}$ , and the protective performance decreases. When the current density continues to increase to 30 A/dm<sup>2</sup>, the resistance–capacitance arc radius of the composite coating decreases, the charge transfer resistance value is reduced to 1245  $\Omega\cdot\text{cm}^{-2}$ , and the corrosion protection performance of the coating on the workpiece is further reduced.

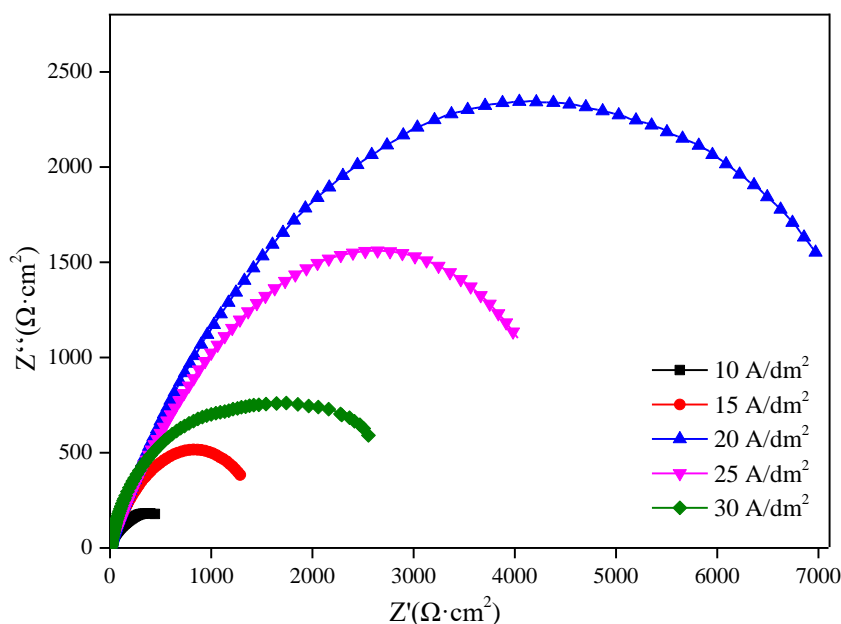


**Figure 9.** Nyquist diagrams of the coatings prepared under different current densities

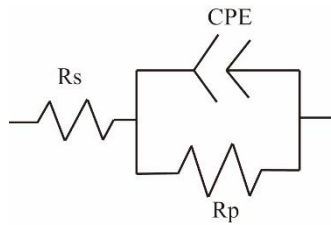


**Figure 10.** AC impedance equivalent circuit diagram of Ni–CeO<sub>2</sub> nanocomposite coatings prepared under different current densities in a 3.5% NaCl solution

**Table 5.** Fitted corrosion parameters for Ni–CeO<sub>2</sub> composite coatings

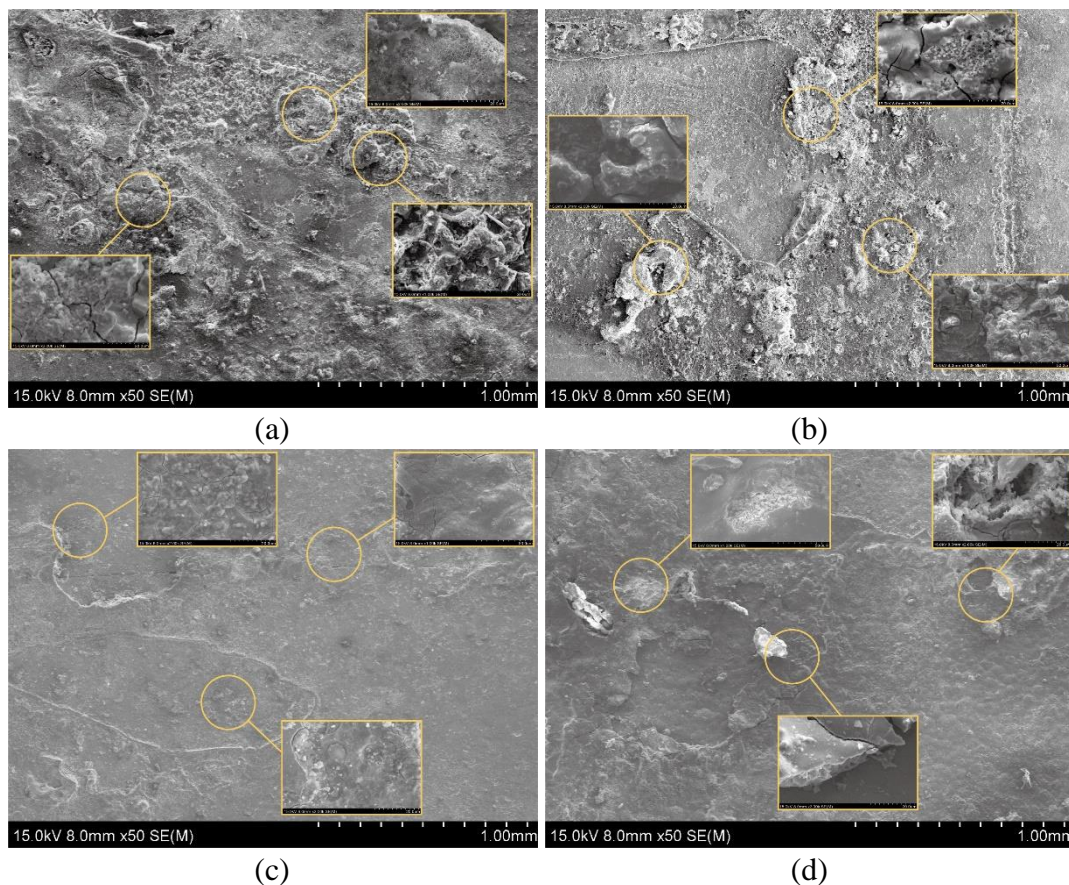
Current density for coating preparation (A/dm <sup>2</sup> )	R <sub>s</sub> (Ω·cm <sup>-2</sup> )	CPE-T	CPE-P	R <sub>p</sub> (Ω·cm <sup>-2</sup> )
10	4.899	1.4538×10 <sup>-2</sup>	0.75354	587
15	1.301	7.7039×10 <sup>-5</sup>	0.75	1556
20	5.056	1.2087×10 <sup>-3</sup>	0.7449	2467
25	4.426	1.6882×10 <sup>-4</sup>	0.68884	2120
30	2.318	1.0565×10 <sup>-4</sup>	0.74557	1245

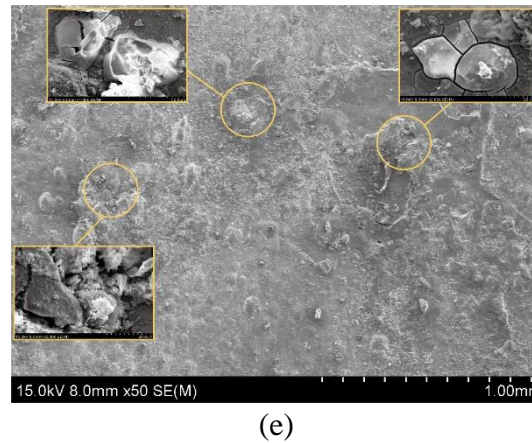
### 3.6.3. Corrosion morphologies

Figure 11 shows the corrosion morphologies of the Ni–CeO<sub>2</sub> composite coatings prepared under different current densities after being immersed in a 3.5% NaCl solution for 24 h. Figure 11(a) shows the surface morphology of the composite coating prepared under a current density of 10 A/dm<sup>2</sup> after corrosion. The partial figure shows a large number of corrosion pits and cracks on the corrosion surface of the coating and traces of corrosion peeling. Due to the effect of hydrogen evolution [42] on the composite coating prepared at a low current density, the surface is uneven, and the coating has poor compactness. Moreover, it exhibits local pitting corrosion in the corrosive medium, causing the coating surface to fall off; cracks and workpiece failure can be confirmed. As shown in Figure 11(b), the surface of the composite coating prepared at a current density of 15 A/dm<sup>2</sup> is better than that of the coating prepared at a current density of 10 A/dm<sup>2</sup> after corrosion; however, there are still corrosion pits and corrosion cracks due to pitting corrosion [43]. Nevertheless, increasing the current density improves the surface appearance of the coating. This is conducive to the corrosion protection performance of the coating for the workpiece; the corrosion morphology shown in Figure 11(c) is relatively flat without any evident pits. Through the local detailed diagram, it can be seen that the corrosion mechanism at this time is mainly uniform corrosion [44]. The composite coating prepared at a high density has a smaller crystal grain size under the MHD effect, the nano-cerium oxides that adsorb the other ions on the coating surface are regularly arranged, and the coating structure is uniform and compact. This effectively hinders the formation of corrosion sites of Cl<sup>-</sup> ions on the coating surface, and pitting corrosion is transformed to uniform corrosion. Figure 11(d) shows that when the current density increases to 25 A/dm<sup>2</sup>, a large

surface shedding area can be seen at the corrosion interface, cracks and faults can be observed due to corrosion, the current density increases, the flatness of the coating surface decreases,  $\text{Cl}^-$  corrosion sites are formed on the coating surface, and the local corrosion is serious. This leads to a peeling off of the coating surface [45] and a decrease in the corrosion resistance of the coating. When the current density of the composite coating continues to increase to  $30 \text{ A/dm}^2$ , the surface corrosion (Figure 11(e)) becomes more severe. There is a partial peeling off of the coating on the surface, and severe pitting and corrosion cracks can be seen on the partial map. This is because of the deterioration in the surface flatness and compactness of the composite coating prepared under a higher current density, which is beneficial to the formation of a large number of corrosion sites on the surface of  $\text{Cl}^-$ . Moreover, the corrosion protection provided by the coating for the workpiece is significantly weakened, and the workpiece gradually fails.

In summary, the corrosion resistance of the composite coating mainly depends on the density, matrix properties, surface roughness, particle properties, and distribution state of the coating. When the current density is  $20 \text{ A/dm}^2$ , the content of each element entering the coating increases, and the MHD effect promotes the regular arrangement of the nano- $\text{CeO}_2$  particles inside the coating. The prepared composite coating has good compactness, high surface flatness, and a layer of protection against oxidation. The film effectively hinders the formation of corrosion sites, the pitting corrosion is transformed to a uniform corrosion, and the corrosion resistance of the coating is excellent.





(e)

**Figure 11.** Microstructures of corroded Ni–CeO<sub>2</sub> composite coatings prepared at current densities of: (a) 10 A/dm<sup>2</sup>, (b) 15 A/dm<sup>2</sup>, (c) 20 A/dm<sup>2</sup>, (d) 25 A/dm<sup>2</sup>, (e) 30 A/dm<sup>2</sup>

#### 4. CONCLUSION

Ni–CeO<sub>2</sub> composite coatings were prepared by jet electrodeposition technology with the aid of a vertical magnetic field. The effects of processing current density on the micromorphology, microhardness, structure, composition, and wear resistance of the composite coatings were explored. The following conclusions can be drawn from the study results:

(1) When the composite coating was prepared using the magnetic field-assisted jet electrodeposition, the MHD effect produced by the magnetic field provided a washing effect on the workpiece surface, resulting in fewer defects on the coating surface. When the current density was increased to 20 A/dm<sup>2</sup>, the composite coating had the least number of surface defects, good compactness, high surface flatness, and best surface quality.

(2) The introduction of a vertical magnetic field facilitated the entry of nano-CeO<sub>2</sub> particles into the coating and the formation of amorphization. Therefore, the prepared Ni–CeO<sub>2</sub> composite coating exhibited an amorphous structure. With the increase in the processing current density, the contents of Ni and Ce elements in the coating increased first and then decreased. At 20 A/dm<sup>2</sup>, the content of Ni reached its maximum, and at 25 A/dm<sup>2</sup>, the content of Ce reached its maximum.

(3) The application of a vertical magnetic field was found to be conducive to the regular ordering of the nano-CeO<sub>2</sub> particles. With the increase in the current density of the composite coating, the strengthening and dispersion of the nano-CeO<sub>2</sub> particles in the coating were improved, and the microhardness of the composite coating was significantly enhanced. When the current density was 20 A/dm<sup>2</sup>, the composite coating exhibited a maximum microhardness value of 665.78 HV<sub>0.1</sub>.

(4) With the increase in the current density, the width, depth, and cross-sectional area of the wear scars in the composite coating surface first decreased and then increased. At a low current density, the composite coating was thinner, and its hardness value was low. The coating was worn due to severe adhesive wear; with the increase in the current density, the coating underwent slight oxidative wear and abrasive wear. When the current density of the composite coating was increased to 20 A/dm<sup>2</sup>, the coating surface showed less wear.

(5) The introduction of a vertical magnetic field was found to be conducive to the regular ordering of the particles in the coating, and under an appropriate current density, the strengthening and dispersion of the fine grains made the coating surface to exhibit good flatness, good compactness, and transformation of pitting corrosion to uniform corrosion. The coating exhibited excellent corrosion protection performance for the substrate. The composite coating prepared at a current density of 20 A/dm<sup>2</sup> exhibited the lowest self-corrosion current and corrosion rate in a 3.5% NaCl solution and the highest self-corrosion voltage, thus demonstrating its excellent corrosion protection performance.

#### ACKNOWLEDGEMENTS

Financial support for this work was provided by the Fundamental Research Funds for the Central Universities (Grant number KYXJ202002), the National Natural Science Foundation of China (Grant number 31901455), the Natural Science Foundation of Jiangsu (Grant number SBK2018041878), the Postdoctoral fund of China (Grant number 2018M632314), Nanjing Agricultural University Innovation Training Plan (Grant number 202030XX42), Innovation Training Plan for College Students of Jiangsu (Grant number 202010307154Y).

#### References

1. S.G. Guo, L. Wang, Y.H. Jin, N. Piao, Z.H. Chen, G.Y. Tian, J.G. Li, C.C. Zhao and X.M. He, *Nano Convergence*, 7 (2020) 21.
2. J. Cao, L. Wang, X.M. He, M. Fang, J. Gao, J.J. Li, L.F. Deng, H. Chen, G.Y. Tian, J.L. Wang and S.S. Fan, *J. Mater. Chem. A*, 1 (2013) 5955.
3. M. Sun, N. Zhang, H.M. Kan, X.Y. Wang, F.Y. Yang and T.T. Fu, *Adv. Mater. Res.*, 690-693 (2013) 458.
4. L. Benea, P.L. Bonora, A. Borello, S. Martelli, F. Wenger, P. Ponthiaux and J. Galland, *J. Electrochem. Soc.*, 148 (2001) C461.
5. L. Benea, *Mater. Manuf. Processes*, 14 (1999) 231.
6. Y.W. Yao, H.S. Dong, L.M. Jiao, N.C. Yu and L. He, *Trans. Electrochem. Soc.*, 163 (2016) D179.
7. Y.Y. Xu, Y.J. Xue, F. Yang, C.Y. Liu and J.S. Li, *Appl. Mech. Mater.*, 395-396 (2013) 174.
8. L.B. Wang, S.L. Xing, H.B. Liu, C.H. Jiang and V. Ji, *Surf. Coat. Technol.*, 399 (2020) 126119.
9. Y.H. Lei, Z.C. Qiu, N. Tan, H.L. Du, D.D. Li, J.R. Liu, T. Liu, W.G. Zhang and X.T. Chang, *Prog. Org. Coat.*, 139 (2020) 105430.
10. S. Uhm, Y. Yi and J. Lee, *Catal. Lett.*, 138 (2010) 46.
11. D.W. Chu, Y. Masuda, T. Ohji and K. Kato, *Phys. Status Solidi A*, 209 (2012) 139.
12. G. Fasol and K. Runge, *Appl. Phys. Lett.*, 70 (1997) 2467.
13. O.Y. Gorobets, V.Y. Gorobets, D.O. Derecha and O.M. Brukva, *J. Phys. Chem. C*, 112 (2008) 3373.
14. K. Subramanyam, N. Sreelekha, D. A. Reddy, M. Ramanadha, B. Poornaprakash, K. C. Reddy, R.P. Vijayalakshmi, *Ceram. Int.*, 46 (2020) 5086.
15. R. Peipmann, J. Thomas, A. Bund, *Electrochim. Acta*, 52 (2007) 5808.
16. C. Wang, Y.B. Zhong, J. Wang, Z.Q. Wang, W.L. Ren, Z.S. Lei and Z.M. Ren, *J. Electroanal. Chem.*, 630(2009) 42.
17. Y.D. Yu, G.Y. Wei, H.L. Ge, L. Jiang, L.X. Sun, *Surf. Eng.*, 33 (2017) 483.
18. R. Morimoto, A. Sugiyama and R. Aogaki, *Electrochemistry*, 72 (2004) 421.
19. M. Chipara, R. Skomski and D.J. Sellmyer, *Mater. Lett.*, 61 (2007) 2412.
20. Z.L. Wang, G.R. Li, J.H. Liang and Y.X. Tong, *ChemPhysChem*, 12 (2011) 166.

21. R.N. Bhattacharya, S. Phok, Y.L. Xu and R. Bhattacharya, *IEEE Trans. Appl. Supercond.*, 7 (2007) 3321.
22. N.S. Qu, X.Y. Hu, W.H. Qian, Z.W. Zhu, *Surf. Eng.*, 30 (2014) 159.
23. M. Sedighi, A. A. Rostami, E. Alizadeh, *Int. J. Hydrogen Energy*, 42 (2017) 4998.
24. A.T. Apostolov, I.N. Apostolova, J.M. Wesselinowa, *Physica E*, 124 (2020) 114364.
25. B.S. Li, W.W. Zhang, D.D. Li and J.J. Wang, *Mater. Chem. Phys.*, 229 (2019) 495.
26. C. Wang, L. Shen, M.B. Qiu, Z.J. Tian and W. Jiang, *J. Alloys Compd.*, 727 (2017) 269.
27. R. Han, M.Y. Qi, Z. Mao, X. Lin and P. Wu, *Phys. Lett. A*, 384 (2020) 126526.
28. P. H. Ho, M. Ambrosetti, G. Groppi, E. Tronconi, G. Fornasari, A. Vaccari and P. Benito, *Catal. Today*, 334 (2019) 37.
29. Z.G. Yang, Z.Q. Yin, Z.J. Zhao, J.B. Yu, J.Y. Li, Z.M. Ren and G. Yu, *Mater. Chem. Phys.*, 240 (2020) 122148.
30. K.O. Nayana, S. Ranganatha, H.N. Shubha and M. Pandurangappa, *Trans. Nonferrous Met. Soc. China*, 29 (2019) 2371.
31. S. Shanmugasamy, K. Balakrishnan, A. Subasri, S. Ramalingam and A. Subramania, *J. Rare Earths*, 36 (2018) 1319.
32. N.S. Qu, D. Zhu and K.C. Chan, *Scr. Mater.*, 54 (2006) 1421.
33. L.R. Kanyane, K. Gandazha, O. S. I. Fayomi and A.P.I. Popoola, *Procedia Manuf.*, 35(2019)814.
34. M. Srivastava, V. K. William Grips and K. S. Rajam, *Appl. Surf. Sci.*, 257 (2010) 717.
35. L.B. Wang, Y.T. Zhao, C.H. Jiang, V. Ji, M. Chen, K.Zhan and F. Moreira, *J. Alloys Compd.*, 754 (2018) 93.
36. J.L. Wang, R.D. Xu and Y.Z. Zhang, *Trans. Nonferrous Met. Soc. China*, 20 (2010) 839.
37. A. K. Chaudhari and V. B. Singh, *Arabian J. Chem.*, 12 (2019) 5028.
38. B.S. Li, W.W. Zhang, D.D. Li and J.J. Wang, *Mater. Chem. Phys.*, 2291 (2019) 495.
39. T.F. Xiang, M.X. Zhang, C. Li, C.D. Dong, L. Yang and W.M. Chan, *J. Alloys Compd.*, 736 (2018) 62.
40. K. Aggoun, L. Chaal, J. Creus, R. Sabot, B. Saidani and M. Jeannin, *Surf. Coat. Technol.*, 372 (2019) 410.
41. X. Liu, T. C. Zhang, H.Q. He, L.K. O.Y. and S.J. Yuan, *J. Alloys Compd.*, 834 (2020) 155210.
42. L.B. Wang, M. Chen, H.B. Liu, C.H. Jiang and V. Ji, Florent Moreira, *Surf. Coat. Technol.*, 331 (2017) 196.
43. B.S. Li, D.D. Li, T.Y. Mei and W.W. Zhang, *Results Phys.*, 13 (2019) 102375.
44. C.D. Chen, S.G. Dong, R.Q. Hou, J. Hu, P.L. Jiang, C.Q. Ye, R.G. Du and C.J. Lin, *Surf. Coat. Technol.*, 326 (2017) 183.
45. Y.J. Xue, H.B. Liu, M.M. Lan, J.S. Li and H. Li, *Surf. Coat. Technol.*, 204 (2010) 3539.